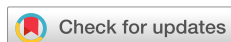


RESEARCH ARTICLE | FEBRUARY 15 2024

Estimates of global recycling coefficients for LTX- β discharges

Special Collection: *Papers from the 64th Annual Meeting of the APS Division of Plasma Physics*

A. Maan  ; D. P. Boyle  ; R. Majeski  ; G. J. Wilkie  ; M. Francisquez  ; S. Banerjee  ; R. Kaita  ; R. Maingi  ; B. P. LeBlanc  ; S. Abe  ; E. Jung  ; E. Perez  ; W. Capecchi  ; E. T. Ostrowski  ; D. B. Elliott  ; C. Hansen  ; S. Kubota  ; V. Soukhanovskii  ; L. Zakharov 



Phys. Plasmas 31, 022505 (2024)
<https://doi.org/10.1063/5.0177604>



Articles You May Be Interested In

Kinetic modeling of neutral transport for a continuum gyrokinetic code

Phys. Plasmas (May 2022)

Effect of neutral interactions on parallel transport and blob dynamics in gyrokinetic scrape-off layer simulations

Phys. Plasmas (November 2023)

Analysis of neutral particle recycling and pedestal fueling in a H-mode DIII-D discharge

Phys. Plasmas (February 2010)

Estimates of global recycling coefficients for LTX- β discharges

Cite as: Phys. Plasmas 31, 022505 (2024); doi: 10.1063/5.0177604

Submitted: 22 September 2023 · Accepted: 23 January 2024 ·

Published Online: 15 February 2024



A. Maan,^{1,a,b)} D. P. Boyle,¹ R. Majeski,¹ G. J. Wilkie,¹ M. Francisquez,¹ S. Banerjee,¹ R. Kaita,¹ R. Maingi,¹ B. P. LeBlanc,¹ S. Abe,¹ E. Jung,¹ E. Perez,² W. Capecci,³ E. T. Ostrowski,⁴ D. B. Elliott,⁵ C. Hansen,⁶ S. Kubota,⁷ V. Soukhanovskii,⁸ and L. Zakharov⁹

AFFILIATIONS

¹Princeton Plasma Physics Laboratory, Princeton, New Jersey 08536, USA

²Nuclear Engineering and Engineering Physics, University of Wisconsin, Madison, Wisconsin 53706, USA

³Department of Physics, University of Wisconsin, Madison, Wisconsin 53706, USA

⁴Chemical and Biological Engineering, Princeton University, Princeton, New Jersey 08540, USA

⁵Oak Ridge National Laboratory, Oak Ridge, Tennessee 37830, USA

⁶Applied Physics and Applied Mathematics, Columbia University, New York, New York 10027, USA

⁷Physics and Astronomy, University of California, Los Angeles, California 90095, USA

⁸Lawrence Livermore National Laboratory, Livermore, California 94550, USA

⁹LiWall Fusion, Princeton, New Jersey 08543, USA

Note: This paper is part of the Special Collection: Papers from the 64th Annual Meeting of the APS Division of Plasma Physics.

Note: Paper UI1 3, Bull. Am. Phys. Soc. 67 (2022).

^{a)}Invited speaker.

^{b)}Author to whom correspondence should be addressed: amaan@pppl.gov

ABSTRACT

We report the first observation of global recycling coefficient R near 0.5 in the Lithium Tokamak eXperiment- β (LTX- β), significantly below the minimum R previously reported in other devices. In a series of experiments with varied Li wall conditioning, estimates of the recycling coefficient have been made using a Lyman- α array and DEGAS2 modeling. A progressive reduction in Lyman- α emission with increased lithium and an increase in edge electron temperature are observed. It is also observed that with increasing Li coating thickness, the effective particle confinement time τ_p^* is reduced and approaches TRANSP calculated energy confinement time (τ_E), with τ_p^* near $\tau_{E,TRANSP}$ for the lowest recycling coefficients. Edge temperatures approaching core plasma temperatures, first reported in LTX, can now be directly connected to estimates of the recycling coefficient and qualitatively agree with previous UEDGE simulations. The particle flux to the limiting surfaces appears to be significantly reduced in comparison with fluid scrape-off layer (SOL) models, indicating that a large fraction of the SOL ions are mirror trapped. SOL collisionality drops more than an order of magnitude below the banana regime boundary, indicating the importance of kinetic effects. Full-f 1x2v gyrokinetic simulations of SOL field lines with the GKEYLL code indicate that the fraction of ions trapped along field lines increases as collisionality drops, as a result of increased lithium evaporation.

© 2024 Author(s). All article content, except where otherwise noted, is licensed under a Creative Commons Attribution (CC BY) license (<http://creativecommons.org/licenses/by/4.0/>). <https://doi.org/10.1063/5.0177604>

I. INTRODUCTION

Plasma material interactions (PMIs) with the first wall of a tokamak, specifically the first few hundred nanometers with which the plasma interacts, have a strong influence on global plasma performance.¹ Practical nuclear fusion reactors are also required to exhaust many megawatts per squared meter of heat flux at the wall in addition to withstanding damage from charged particles and neutrons from the

plasma. Plasma-facing components (PFCs) are generally classified as high Z or low Z, where Z is the average atomic number of the wall material. High Z refractory metals, such as tungsten,² molybdenum, and their alloys, are the leading candidates for tokamak PFCs due to low sputtering yields and high heat flux tolerance. However, the ingress of even small amounts of high Z impurities into the core can severely degrade plasma performance. This is mostly due to the fact

that high Z ions can undergo many excitation processes before they are fully stripped of electrons, leading to excessive radiative power loss. Extra bursts of heat and particles from instabilities such as edge-localized modes (ELMs) or disruptions can not only lead to extra impurity influx, but also cause catastrophic damage by melting or cracking PFCs.

Low Z PFCs, particularly low Z liquid lithium PFCs, can be an attractive alternative, as much higher levels of impurities can be tolerated by the core plasma while maintaining fusion power output. The main disadvantage of low Z PFCs is the greater sputtering and loss of material from the first wall. A layer of flowing liquid lithium on top of high Z PFCs can be used to redistribute lost material and to allow external process to remove retained tritium.^{3–5} A liquid surface would also be much more resilient to extra heat loads through evaporative and radiative shielding. Because lithium has high chemical reactivity, it can also be used to capture impurities commonly present in a vacuum vessel such as water. Lithium offers another advantage over other candidates with low Z in the form of gettering and retention of hydrogen and its isotopes.⁶

Hydrogen from the plasma along open field lines in the scrape-off layer of a tokamak interacts with the walls and can be reflected or desorbed from the wall as cold neutrals or retained in the walls by some mechanism. The cold neutrals close to the walls of the tokamak act as an energy sink and cool the plasma down at the edge. The retention of hydrogen and its isotopes in a PFC is usually quantified in terms of wall recycling (R), defined as the ratio of flux of hydrogen neutrals from the wall to the scrape-off layer (SOL), to the flux of hydrogen ions from the plasma to the walls. It has long been theorized that a plasma with low recycling walls can sustain a high edge temperature and even completely flat temperature profiles from the core to the edge.^{12–14} Even moderate reduction in recycling has shown to reduce the drive for edge-localized modes in H-mode plasmas and improve confinement in NSTX.¹⁵ Based on neoclassical predictions,^{16,17} the strongest transport process in the core is the ion thermal conduction or the ion radial heat flow. It is stronger (i.e., faster) than every other processes by a factor of $\frac{m_i}{m_e}$, where m_i and m_e are ion and electron mass, respectively. Ion thermal conduction has an ion temperature gradient dependence.¹⁴ Ion and electron temperature gradient-based instabilities are also among the drivers of anomalous transport.¹⁸ Therefore, eliminating temperature gradients (i.e., having flat temperature profiles) can mitigate such transport.¹³ Density gradients, however, should persist in such a regime since particle transport will account for most of the energy transport from the plasma.

While numerous facilities^{19–26} have studied and demonstrated various benefits of lithium as a first wall, the Lithium Tokamak eXperiment (LTX) and its successor the Lithium Tokamak eXperiment- β (LTX- β), depicted in Fig. 1 uniquely explore confinement and general plasma performance improvement due to near complete coverage of high Z PFCs with evaporative lithium coatings thicker than the maximum expected ion implantation depth from the plasma. LTX documented the first demonstration of flat electron temperature profiles.²⁷ These discharges were documented to have a Z_{eff} of around 1.2, well below $Z_{eff} > 2$ for most metal and carbon-walled machines.²⁸ The LTX- β device, the successor of LTX, began operations in 2017. LTX- β is a low-aspect-ratio tokamak with major radius 0.4 m and minor radius 0.26 m. The vacuum vessel houses a shell, divided into four quadrants, conformal to the shape of the largest plasma that

fits in the volume. The shell is 1-cm-thick copper, clad with 1.5-mm-thick explosively bonded stainless steel on the plasma-facing side, and the copper surfaces are nickel plated to avoid damage from lithium interaction. The PFCs of LTX- β were conditioned by vacuum baking the shells up to 250 °C, occasionally up to 300 °C, and glow discharge conditioning using neon; prior to lithium evaporation, the shells are depicted in Figs. 1 and 3. The transition from stainless steel walls to lithium coatings and consequent improvement in plasma performance is documented in earlier work.^{29,30}

Two evaporators, placed at the midplane at diametrically opposite toroidal positions, are used to coat > 95% of the PFCs with fresh lithium.^{11,31} Regularly coating the walls of LTX- β results in unique vacuum conditions, as demonstrated in Fig. 2. The figure shows the spectrum of impurities in the LTX- β vacuum vessel; the data are averaged over several days to show minor features. The vessel's vacuum is primarily comprised of hydrogen and nitrogen, likely from a small air leak. Water is only present in trace amounts, unlike other tokamaks, where it is often one of the main impurities. This is due to the fact that lithium coatings on the shells act as a continuous and active getter of vacuum impurities. Lithium specifically getters water vapor and retains it as a mixed oxide-hydroxide^{32,33} while releasing hydrogen gas. Because the lithium coatings are actively pumping impurities from the residual vacuum and plasma, they evolve. The evolution is mostly to lithium oxide and lithium hydroxide in LTX- β .³⁰ Such evolution brings with it a degradation in plasma performance. The degradation is linked to the loss of ability of lithium coatings to sequester impurities and retain hydrogen from the plasma. The loss of impurity sequestration is indicated by the relative increase in oxygen line emission to plasma density³⁴ and lack of reduced recycling is indicated by increasing plasma density decay times after a puff and a general rise of Lyman- α emission from the plasma.¹¹ Therefore, repeatedly coating the walls of LTX- β with fresher lithium coatings is needed to regain performance. Such partially oxidized lithium coatings are referred to as passivated lithium coatings. The longer the time since the last evaporation, the greater the degree of passivation. However, it should be noted that minor oxidation to Li₂O is expected and inevitable after lithium deposition. The degradation in plasma performance is starker once these coatings start evolving to LiOH; in LTX and LTX- β , this transition takes at least a few weeks, given the near ultrahigh vacuum conditions.^{34,35}

The remainder of this paper discusses changes in recycling starting from passivated lithium coatings and continuing through multiple subsequent lithium evaporations. In Sec. II, discharges are compared across two datasets, referred to as the similar fueling dataset and the similar density dataset. The similar fueling dataset compares a baseline discharge that has partially passivated lithium walls to two other discharges with increasingly more lithium deposited onto the shells, while programming for coil currents and gas fueling is kept constant. A discharge refers to an ensemble average of ~30 identical shots, and the shots were repeated to demonstrate reproducibility and collect statistics on various diagnostics. The similar density dataset compares the passivated lithium baseline discharge to two other discharges, again with increasing lithium, but where extra fueling is used to match the line-averaged density of the passivated lithium discharge. Density decay times of the discharges are compared in addition to wall pumping factor and Thomson scattering (TS) profiles at peak density. Next, in Sec. III, Lyman- α emission measurements are compared and used to constrain estimates of the global recycling coefficient using

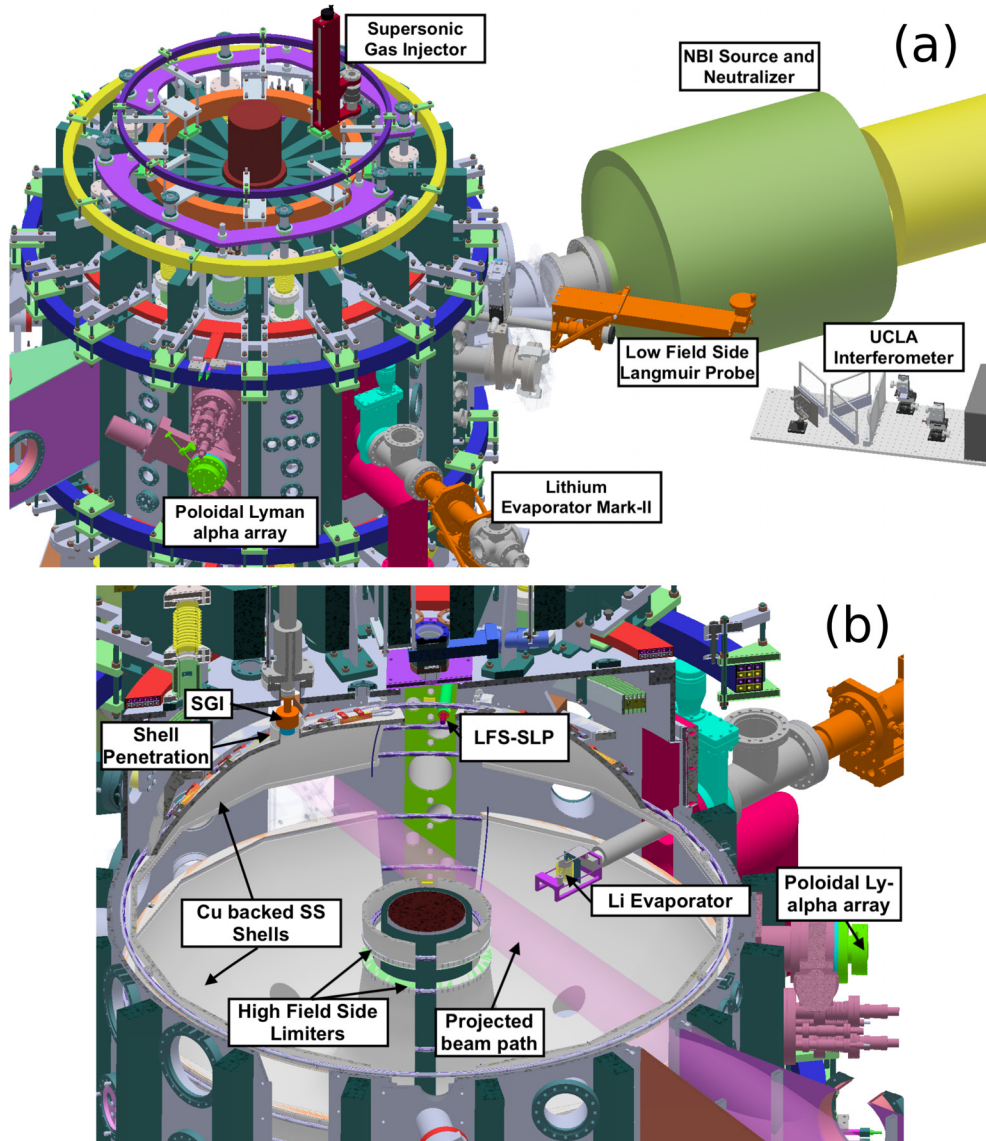


FIG. 1. (a) Shows the LTX- β tokamak, the locations of the Neutral Beam Injector^{7,8} for beam fueling and heating studies, the millimeter-wave interferometer for plasma density measurements,⁹ the low-field-side single-swept Langmuir probe (LFS-SLP) for plasma edge density and temperature measurements, supersonic gas injector (SGI)¹⁰ for fueling and density decay measurements at the wall, second-generation (Mark-II) LTX- β lithium evaporators for depositing lithium on the PFCs, and the poloidal Lyman- α array for recycling analysis¹¹ are shown. (b) Shows the internal view of the diagnostics and operational subsystems depicted in (a); additionally, the copper-backed stainless steel PFCs and the high-field-side limiters are annotated.

15 January 2025 17:36:27

DEGAS2 modeling. LTX- β diagnostics and operational subsystems utilized for this analysis are shown in Figs. 1 and 3. A comparison of the convergence of particle and energy confinement times also demonstrates a change from thermal conduction losses to particle convection losses as recycling is reduced. A similar comparison in discharges with modest neutral beam fueling is also presented. Finally, in Sec. IV, the paper concludes with a discussion of SOL transport under low collisionality hot-edge conditions that exist for these low recycling discharges, including initial gyrokinetic simulations of open field lines using Gkeyll.

II. IMPROVEMENT IN DISCHARGE PERFORMANCE WITH LITHIUM EVAPORATION

To study changes in discharge characteristics as a function of wall conditions, a baseline discharge with partially passivated lithium walls is selected, LTX- β shot numbers 103764-827. The passivated lithium baseline discharge is initiated on walls that have a \sim 5-week-old coating of lithium. Based on previous experience with discharges and surface analysis using old discharges, it is expected that the surface was well oxidized and partially hydroxidized.^{18,34} The previous coating had an average lithium thickness of about 50 nm. Plasma current measured by

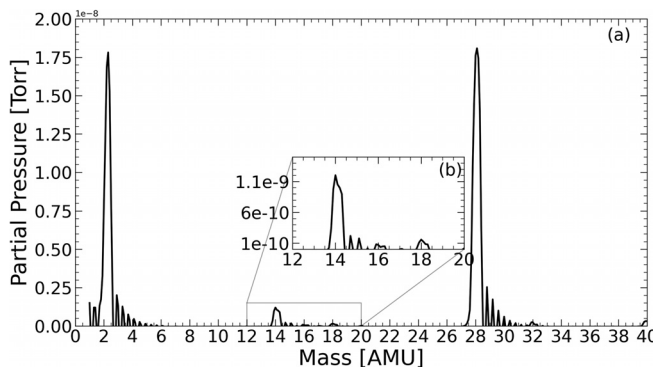


FIG. 2. (a) Typical spectrum from a residual gas analyzer (RGA) in LTX- β after many lithium evaporations. The spectrum is averaged over many scans for a period of nearly five days, with a scan every 6 s, to enhance the signal-to-noise ratio and identify trace impurities in LTX- β residual vacuum. During operations, the vacuum vessel is actively chilled to 15 °C. (b) Inset zoom between 12 and 20 AMU, note that water partial pressure is measured to be $\sim 1 \times 10^{-10}$ Torr, forming only 2% of the base vacuum.

the LTX- β I_p Rogowski and line-averaged density measured by the interferometer are shown in Fig. 4. As the LTX- β Thomson scattering (TS) laser fires only a single pulse per discharge, the discharge is repeated ~ 30 times during a single run day, while the TS measurement

time is varied, separated by about 5 min between each discharge. TS data are averaged from several discharges at each measurement time to improve statistics, while all other data are averaged over the full ensemble. Based on equilibrium reconstructions, the discharge breaks down and fills the entire volume of the shells. During peak density, between 460 and 470 ms, the plasma volume is observed to remain fairly steady, the discharges are made to limit on the high-field-side (HFS) limiters as seen in Fig. 3. The discharge then shrinks and collapses on the high field side as the plasma current ramps down.

The discharge is fueled using a relatively slow high field side (HFS), Fig. 3 puffer, and a fast-acting supersonic gas injector (SGI), Figs. 1 and 3. Both injectors use piezoelectric valves that open and close in less than 0.3 ms. The HFS puffer valve is situated outside the vacuum vessel and is connected to a roughly meter-long tube that leads to a radial nozzle a few cm above the high-field-side midplane. Therefore, gas arrives at the plasma a couple of milliseconds after the HFS valve opens, and even after the valve is turned off, it continues to release gas into the vessel for several milliseconds. On the other hand, the SGI valve directly abuts the nozzle, which is itself only a couple of cm long, and therefore, an immediate cessation of fueling is observed as soon as the SGI valve is turned off, with a delay less than 0.5 ms for the remaining gas to reach the plasma. The HFS puffer is used for the vessel prefill before plasma breakdown and the initial set of gas puffs to ramp up and sustain a discharge. Just before peak plasma current, a set of SGI puffs quickly ramp up the density and then hold it roughly

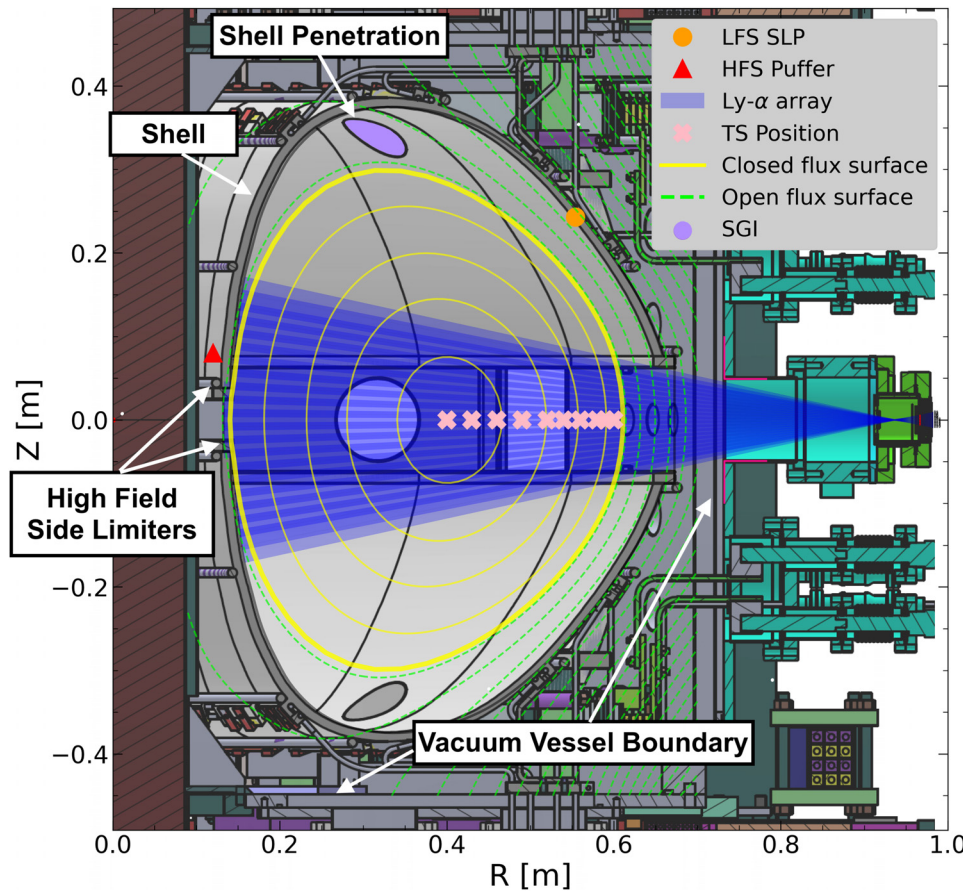


FIG. 3. Poloidal cross section of LTX- β overlaid on a typical reconstruction. The location of the low-field-side Langmuir probe, Thomson scattering positions, and the extent of the Lyman- α array sightlines are shown. The location of the high-field-side limiters and the vacuum vessel boundary are also depicted relative to the diagnostics, along with the poloidal location of the two gas fueling sources.

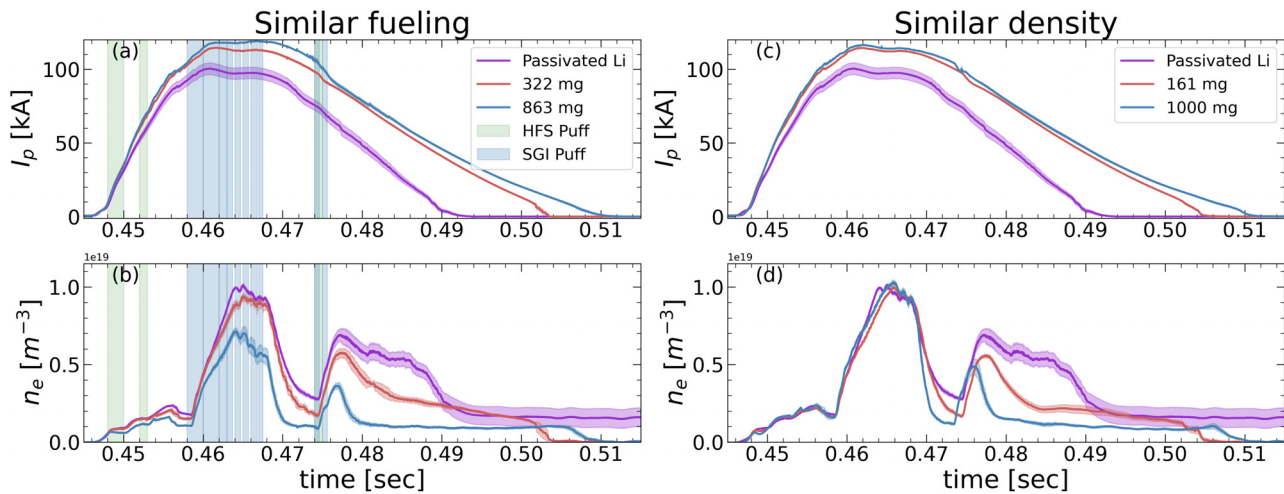


FIG. 4. Ensemble average plasma current (a), line-averaged density (b) for the similar fueling data set, and for the similar density data set (c) and (d). Note that fueling requests for the similar density dataset are not shown. These discharges are later compared at 468 ms, the point of highest density immediately after fueling is terminated.

constant at $\sim 1 \times 10^{19} \text{ m}^{-3}$ for ~ 5 ms, as seen in Fig. 4. The SGI is then completely shut off for several milliseconds in order to monitor the density decay. It is evident that despite aging for 5 weeks before the baseline discharge, the lithium coatings still provide a reduced recycling surface, as density decays rapidly in the absence of external fueling. Some additional gas puffs after the decay restore the density in order to avoid disruptions during the current ramp down, Fig. 4, though they were varied as needed and this part of the discharge is not used in the analysis.

For the similar fueling dataset, the passivated lithium baseline discharge is repeated on two separate run days, first with 322 mg of lithium deposited on the shells (61 nm average thickness, shot numbers 103830-79), and then with an additional 863 mg of lithium (162 nm average thickness, shot numbers 103923-63) [Figs. 4(a) and 4(b)]. Across the three-run days, all field coil and fueling programming is kept constant; the only change corresponds to the extra lithium deposition on the PFCs. For the similar density dataset, the passivated lithium baseline discharge is repeated on two separate run days with 161 mg (30 nm average thickness, shot numbers 107566-614) and 1000 mg (200 nm average thickness, shot numbers 107635-77). All field coil programming is kept constant; however, fueling is increased in order to approximately match the line-averaged density of the passivated lithium case up until peak density. All fueling requests are terminated at 467 ms to quantify changes in density decay across the three-run days. Plasma current- and density-averaged over all discharges in each ensemble are shown in Figs. 4(c) and 4(d).

In general across the two data sets, plasma performance is seen to improve with additional lithium deposition. This improvement is evident in the increase in plasma current as seen in Fig. 4. LTX- β uses a pre-programmed Ohmic loop voltage waveform without feedback; therefore, increased plasma current indicates lower resistivity and better plasma performance via increased temperature and/or lower impurities; reduced impurity emission is also seen in filterscope data.³⁴ It is also common operational observation that as more lithium is evaporated onto the walls, density is reduced when fueling is held constant,¹¹ or alternatively, more gas is needed to sustain a discharge with a

density similar to that of walls with partially passivated lithium on them. This effect on the relationship between density and fueling is attributed to the strong pumping effect of lithium walls and must be related to reduce fueling from hydrogen recycling during a discharge. The relationship between density and fueling can be quantified using what we will call the wall pumping factor, defined here as the ratio of time-averaged plasma density divided by total hydrogen puffed into the vessel, averaged over all the discharges in an ensemble

$$\eta_{wall,i} = \frac{1}{t_{dur,i}} \int_{t=0}^{t=t_{dur,i}} n_e(t) dt / \Gamma_{H_2,i}, \quad \bar{\eta}_{wall} = \sum_{i=0}^K \eta_{wall,i} / K, \quad (1)$$

where $n_e(t)$ is the discharge's line-averaged density measured using the LTX- β interferometer, i is a discharge in a K discharge ensemble, $t_{dur,i}$ is the discharge duration of the i th discharge, and $\Gamma_{H_2,i}$ is the total hydrogen puffed into the tokamak for the i th discharge using both the HFS puffer and the SGI. The normalized wall pumping factor is shown in Fig. 5 for the similar fueling and the similar density data sets. The large reduction in η_{wall} between the partially passivated lithium base case and the 161 mg similar density case can potentially be explained by the fact that these discharges are separated by 11 months of vacuum and plasma operations that included ~ 25 g of lithium deposited onto LTX- β shells for various other experiments.

Fundamentally, recycling can be quantified by the recycling coefficient R , the ratio of recycled particle flux entering the plasma to the total particle flux out of the plasma, $R \equiv \Gamma_{recy}/\Gamma_{out}$. Similarly, the average particle confinement time is essentially the total particle inventory divided by the outward flux, $\tau_p \approx N/\Gamma_{out}$. Combining these quantities with the particle conservation equation that can include external fueling,

$$\frac{dN}{dt} = \Gamma_{ext} + \Gamma_{recy} - \Gamma_{out} \approx \Gamma_{ext} - (1 - R) \frac{N}{\tau_p}. \quad (2)$$

Pumping from external pumps is also ignored since it is much slower, ~ 400 ms characteristic pressure decay time, compared to shot duration and density pumpout due to lithium. In the absence of external

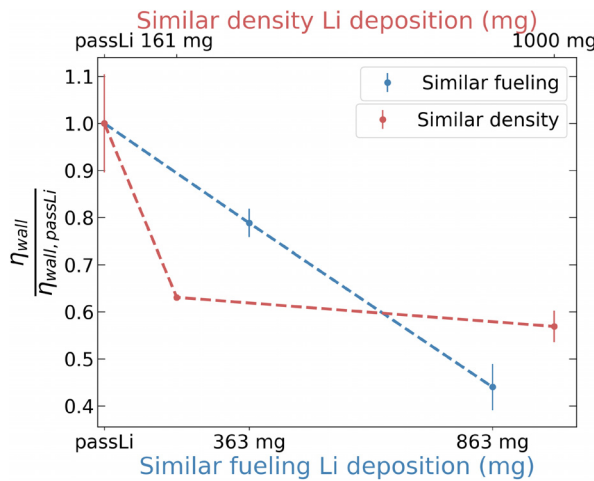


FIG. 5. Discharge ensemble-averaged wall pumping factor as a function of deposited lithium, for the similar fueling data set, on the bottom x axis and for the similar density data set on the top x axis, the values are normalized to the passivated lithium base case, to show a relative increase in wall pumping with increased lithium deposition.

fueling, the effective particle confinement time can be defined and solved using the following expression:

$$\tau_p^* \equiv \frac{\tau_p}{1 - R} \approx -\frac{N}{dN/dt} \quad (3)$$

τ_p^* can therefore be seen as the exponential decay time for the density if all fueling sources are turned off. For a conventional tokamak with

$R \approx 1$, the density decay is expected to be slow. However, as seen in Fig. 4, devices like LTX- β with reduced recycling PFCs exhibit quick density pumpout; in such cases, density decay times can be used as a performance metric.¹⁰ In order to quantify τ_p^* as a function of lithium deposition across the similar fueling and the similar density datasets, fueling is terminated by 467 ms and an exponential decay function is fit to the density waveforms. Figure 6 shows the result of the fits for the two different datasets. As expected, τ_p^* decreases as lithium deposition increases. Interpretation of decreasing τ_p^* in the constant fueling dataset is somewhat complicated by the expectation that τ_p scales with the density.³⁶ However, a consistent reduction in τ_p^* is observed even for the similar density dataset, indicating that such a reduction in the similar fueling dataset can be attributed to a reduction in recycling.

Thomson scattering data are collected for at least four time points each for both cases between 462 and 469 ms. Temperature profiles during the SGI puffs are, in general, peaked. However, for the similar fueling case, at the lowest density and most lithium, the temperature profiles start to broaden after the fueling is terminated as seen in Fig. 7(a), and the ratio $T_e^{\text{edge}}/T_e^{\text{core}}$ for 863 mg in the similar fueling case is ~ 0.6 . The degree of temperature profile relaxation after gas puff termination is less pronounced in the similar density case for both 161 mg and the 1000 mg ensemble. $T_e^{\text{edge}}/T_e^{\text{core}}$ ratios for these two cases are between 0.4 and 0.5.

III. RECYCLING ESTIMATES USING DEGAS2

Emission from excited hydrogen neutrals is proportional to the neutral ionization rate, given fixed plasma parameters, and therefore to the neutral density in a plasma. The LTX- β poloidal Lyman- α array is used to measure Lyman- α emission¹¹ across all cases of the two data sets. Together with forward modeling of neutrals, these measurements allow us to infer neutral production rate. The LTX- β Lyman- α diagnostic is an array of photo-diodes. The photo-diode array is housed in

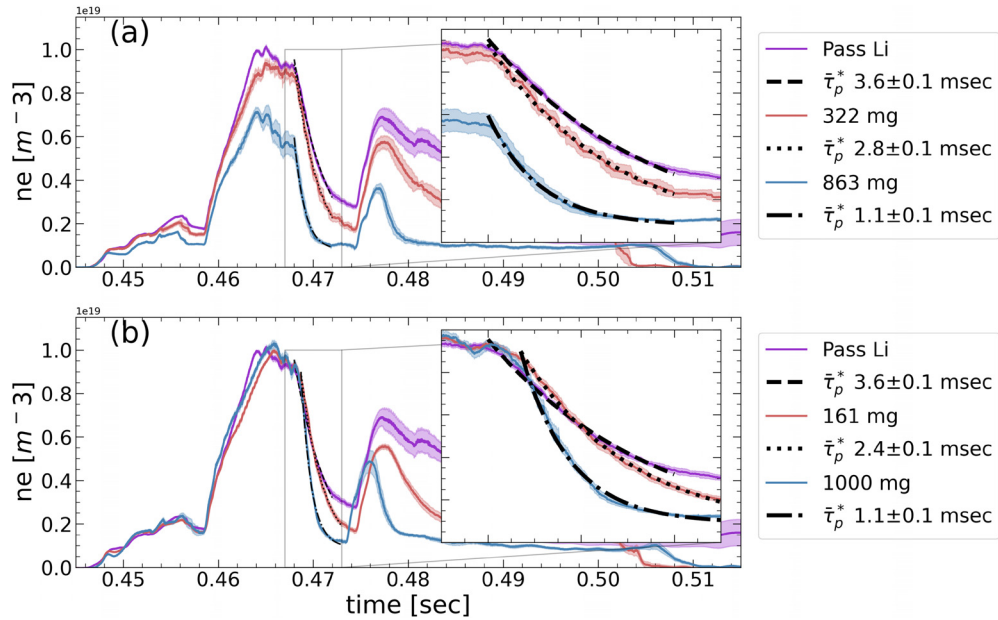


FIG. 6. Average density decay time constants corresponding to the best exponential decay fit for (a) similar fueling and (b) similar density.

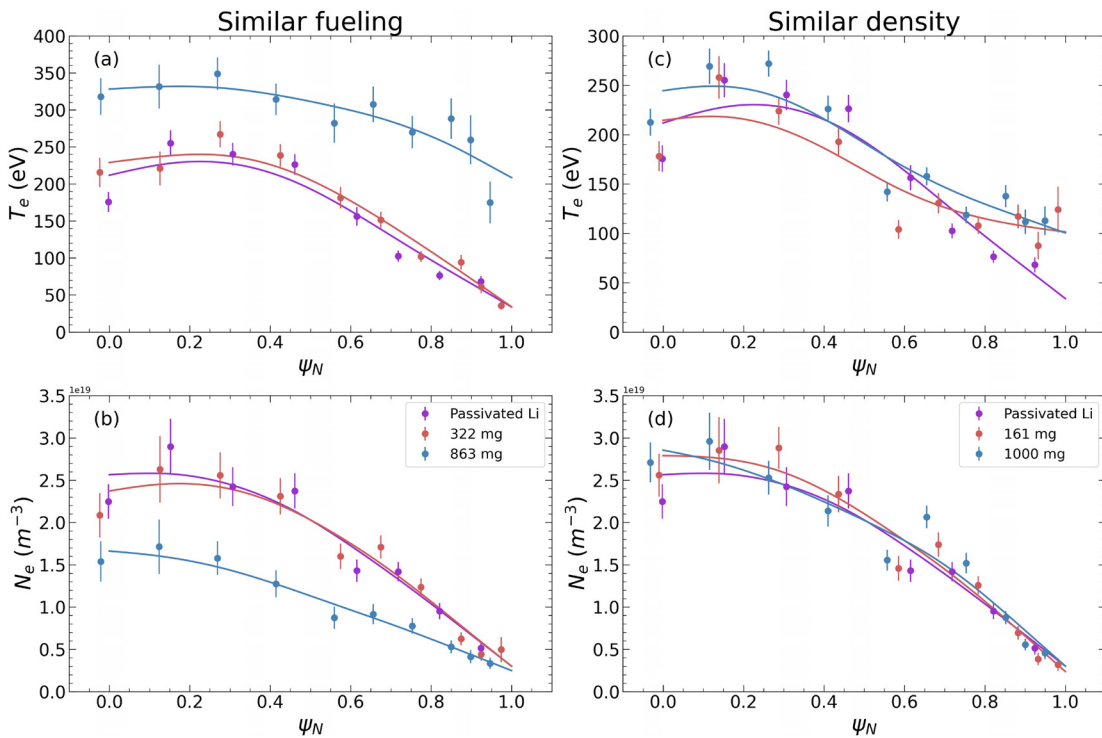


FIG. 7. Plasma electron temperature and density, as measured using the LTX- β Thomson scattering diagnostic at 468 ms, immediately after fueling is terminated, for the similar fueling data set, (a) and (b) and for the similar density data set (c) and (d).

a light-tight can that has a slit-mounted 121-nm narrow-band vacuum ultraviolet (VUV) filter. The array is mounted at the low-field-side (LFS) midplane and looks at the high-field-side limiting edge. Figure 8(a) shows the viewing geometry of all channels relative to an equilibrium reconstruction at 468 ms, immediately after fueling is terminated and

corresponding to the TS profiles in Fig. 7. An innermost and an outermost channel are highlighted, to indicate the viewing geometry of the line integrated signals presented in Figs. 8(b)–8(e). An overall reduction in the Lyman- α emission with increasing lithium evaporation is observed for the similar fueling dataset; the difference is observed to

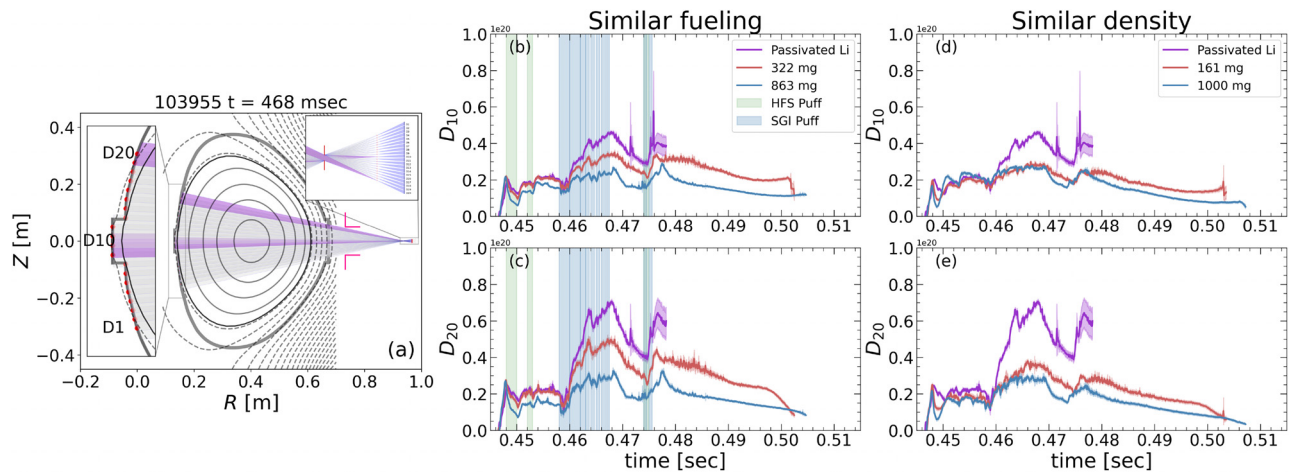


FIG. 8. LTX- β Lyman- α array viewing geometry is depicted in (a) overlaid on the equilibrium reconstruction of the median discharge for similar fueling, 863 mg discharge at 468 ms. Lyman- α array's innermost and outermost channel signals for the similar fueling case are shown in (b) and (c), respectively; and inner and outer channels for the similar density case are depicted in (d) and (e).

persistent even when normalized by density.¹¹ A similar reduction is seen in the similar density dataset.

Recycling is analyzed for these discharges after puffing is terminated, which avoids the unnecessary complexity of modeling transient gas puffing in DEGAS2.³⁷ Due to the fast shutdown of gas from the SGI, the discharges can be compared using DEGAS2 at 468 ms when the density is still high and diagnostic signals are strongest. The plasma geometry is defined by magnetic equilibrium reconstructions, calculated using PSI-TRI³⁸ with pressure kinetically constrained by the TS profiles. Density and temperature are assumed to be constant on closed flux surfaces and interpolated between them, inside the last closed flux surface (LCFS). A low-field-side single-swept Langmuir probe (LFS-SLP) is used to measure plasma density and temperature next to the wall for all the discharges.¹¹ A simple two-point linear interpolation is used to estimate density and temperature in the SOL at the midplane. The density and temperature are then computed along open field lines using Stangeby's sheath-limited model.³⁹ Flux to the surfaces is computed using a simple sound speed approximation, $\Gamma_{\parallel} = n_e c_s$. DEGAS2 simulated neutral density and Lyman- α emission for all five cases are shown in Fig. 9, the corresponding kinetically constrained equilibrium, as calculated by PSI-TRI is overlaid on all figures.

A synthetic Lyman- α array is also included in DEGAS2, with lines of sight of each detector computed using reference values from the LTX- β Lyman- α array geometry.¹¹ DEGAS2 is used to then solve the steady-state kinetic Boltzmann equation for neutral atoms and molecules using the Monte Carlo approach. The shell surface is broken into segments and the plasma core and SOL grid to an unstructured triangular mesh. DEGAS2 tracks line emission and adsorption and calculates a synthetic Lyman- α signal. The DEGAS2 recycling coefficient is then adjusted iteratively as a free parameter until the average level of

emission from the synthetic Lyman- α array matches the value measured by the LTX- β poloidal Lyman- α array.

The DEGAS2 simulations match the Lyman- α measurements well over most of the array, even matching some of the structure of the intensity falloff. However, the simulated profile diverges strongly for the outermost channels both above and below the midplane and these points are therefore excluded from the iterative fit. The disagreement is likely due to a combination of the simplified SOL plasma model used in DEGAS2 and some clipping of the edge channels in the toroidal direction. The clipping likely exists because the array looks at the center stack through a circular port hole and sits behind a 6-in. conflat gate valve. The assumption of linear density and temperature decay from the LCFS to the wall and neglect of SOL mirror trapping is likely a bigger factor here, since it would over-predict both quantities and result in excess calculated emission. To remedy these issues, LTX- β is planning the instrumentation and commissioning of a SOL Thomson scattering system. Additionally, the next iteration of the poloidal Lyman- α array will be made reentrant, therefore have higher coverage on the high field side, and will be calibrated using techniques developed to calibrate the Lyman-Alpha Measurement Apparatus (LLAMA) diagnostic, currently on DIII-D.⁴⁰

Using this method, the direct calculations from DEGAS2 invariably estimated extremely low values of the recycling coefficient, close to 0.2. The simplified SOL plasma model that neglects mirror trapping likely plays a role here, overestimating density on the high field side. Such low values of R are below the irreducible minimum recycling from direct reflections and therefore cannot be taken directly as an absolute measurement. Uncertainties in the absolute calibration of the Lyman- α data may also contribute to the low R values calculated by DEGAS2. In the absence of an available calibrated VUV source,⁴⁰ the

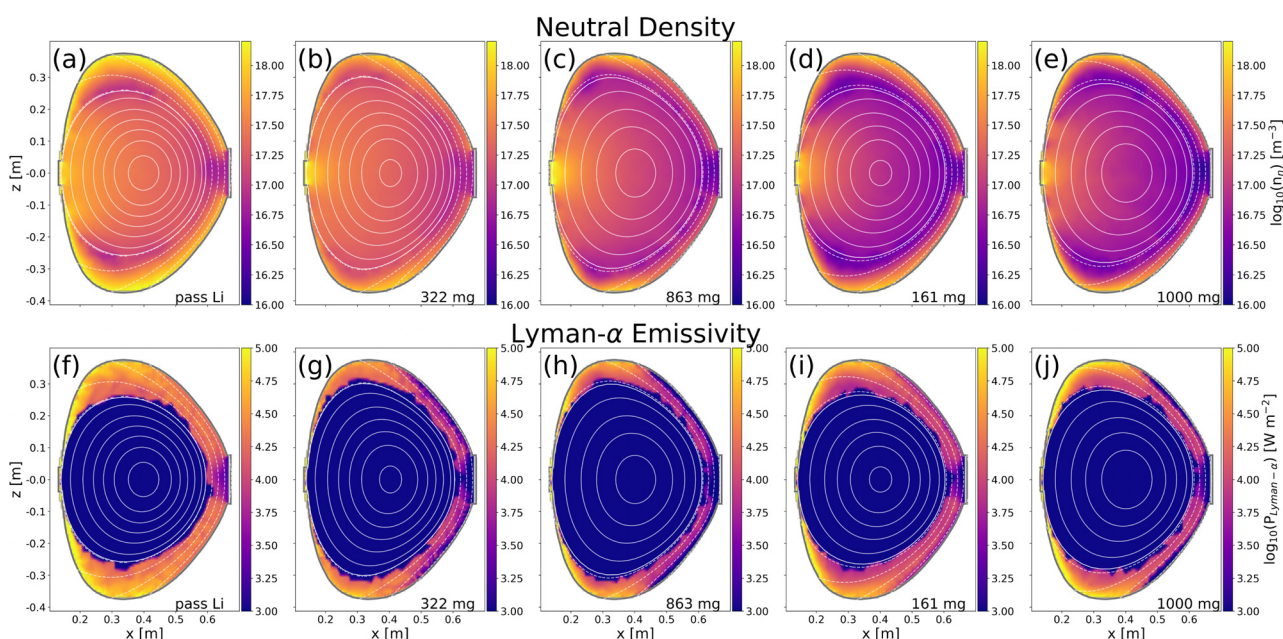


FIG. 9. DEGAS2 simulated neutral hydrogen density, (a)–(e) for the similar fueling discharges, passivated lithium base case, 322 mg, 863 mg and the two similar density discharges, 161 and 1000 mg. (f)–(j) show the DEGAS2 simulated Lyman- α emission map for the same discharges at 468 ms. The corresponding kinetically constrained equilibrium of each discharge is overlaid on all plots.

TABLE I. Summary of estimated global recycling coefficients and density decay times. Recycling coefficients relative to R_D^0 are listed in the column R_{DEGAS2} . Absolute recycling coefficients estimated by including changes in τ_p^* are listed under the R column. Square brackets indicate upper and lower bounds of the estimate.

Case id	Data set	Case	$t_{Li,avg}$ (nm)	$\bar{\tau}_p^*$	R_{DEGAS2}	R
1	Baseline discharge	Passivated Li	50, ~5 weeks old	3.6 ± 0.1	R_D^0	0.87–0.83
2	Similar fueling	322 mg	61	2.8 ± 0.1	$R_D^0 [0.9,1]$	0.85–0.75
3		863 mg	162	1.1 ± 0.1	$R_D^0 [0.65,0.75]$	0.67–0.61
4	Similar density	161 mg	30	2.4 ± 0.1	$R_D^0 [0.65,0.75]$	0.71–0.64
5		1000 mg	200	1.1 ± 0.1	$R_D^0 [0.6,0.7]$	0.56–0.47

calibration is based on the manufacturer's specifications for the diodes and Lyman- α filter. However, as the calibration and modeling uncertainties are expected to affect all of the simulations similarly, the relative recycling coefficients are therefore computed for the dataset. DEGAS2 estimated recycling coefficient is adjusted to fit the Lyman- α data, for the passivated lithium base case; this value is referred to as R_D^0 for the rest of the paper. The resulting relative recycling coefficients are tabulated in Table I under column R_{DEGAS2} . The result of such a fit for the lowest estimated R_{DEGAS2} is depicted in Fig. 10, for the 1000 mg case.

By analyzing all of the datasets together, true global recycling coefficients can be estimated. Experimental scaling of τ_p suggests that it is proportional to density for small Ohmic tokamaks,³⁶ and therefore, for generally similar discharges, $\tau_p \sim CN_e$ has been assumed. This assumption is combined with the relative change in recycling coefficients from DEGAS2 to create a set of nine linear equations with six unknowns, R^i and C, where i is the case number, from Table I. The first set relates τ_p^* to absolute recycling and the second set relates R_D^0 to R^i , $\tau_{p,i}^* = \frac{CN_e}{1-R^i}$, and $\frac{R^i}{R_D^0} = R^i$. The system yields a least squares solution computed using a pseudo-inverse,⁴² listed in Table I. The results show that for these discharges, the recycling coefficient is between 0.47 and 0.87. For the discharges with the most amount of lithium, the global recycling coefficient is found to be ~ 0.6 for the 863 mg discharge and

~ 0.5 for the 1000 mg. For these discharges, the $T_e^{\text{edge}}/T_e^{\text{core}}$ is ~ 0.6 and 0.4, respectively. This ratio is within the range for a global recycling coefficient estimated for LTX, between 0.5 and 0.6, using previously reported UEDGE simulations.²⁷

The neoclassical transport code TRANSP,^{31,43,44} a 1.5D transport solver, is used for interpretive modeling of discharges. The model is constrained by experimental measurements averaged over all shots in an ensemble. TRANSP runs for all five discharge ensembles are constrained using the Thomson scattering measurements between 465 and 470 ms. It is observed that for discharges with the lowest estimated recycling, 863 and 1000 mg, $\bar{\tau}_p^*$ approaches the average $\tau_{E,\text{TRANSP}}$, Fig. 11. Reduction in recycling is expected to reduce conduction losses from the plasma,¹⁴ and since lithium is an excellent getter of impurities, the radiative power loss for these discharges should also be fairly low. The energy in such a case is mostly carried by particles; hence, the particle confinement time should approach the energy confinement times in such a regime.

A small effect on density decay times is also observed with beam fueling across multiple run days. Figure 12 shows a comparison of two discharge ensembles of around ten discharges each. Both fired on the same run day after a 913 mg lithium deposition, corresponding to an average thickness of 170 nm, before the beginning of the run. A 13 kV 30 A hydrogen neutral beam is injected into these discharges at peak density. A discharge that had the maximum reproducible peak density is designed and used for the study, and this is done to reduce beam shine-through and improve beam coupling. A small increase in plasma current is observed with the beam, such increase is seen when there is a beam heating effect and is well documented in recently published beam heating results with low recycling in LTX- β .³¹ With beam fueling, the discharge shows a $\bar{\tau}_p^*$ of ~ 5.3 ms, during the density decay phase. Repeating the discharge without a beam shows a $\bar{\tau}_p^*$ of ~ 4.2 ms, the $\tau_{E,\text{TRANSP}}$ averaged over the density decay times for these two discharges were 2.1 and 2.6 ms, respectively. Consequently, the $\bar{\tau}_p^*$ to $\tau_{E,\text{TRANSP}}$ ratio for the two cases is 1.6–2.5, indicating that these are also fairly low recycling discharges.

IV. IMPLICATIONS OF A LOW COLLISIONALITY SOL

For the five discharge ensembles among the similar fueling and the similar density case, at 468 ms, the midplane to strike point connection length is calculated to be ~ 5.5 m (~ 11 m, strike point to strike point). For the passivated lithium base case, the self-collisional mean free path is estimated to be a third of the strike point to strike point connection length. However, for the low recycling cases, the self-collisional mean free path can be three to ten times the connection length, near the LCFS, in the SOL. Electron collisionality in the SOL,

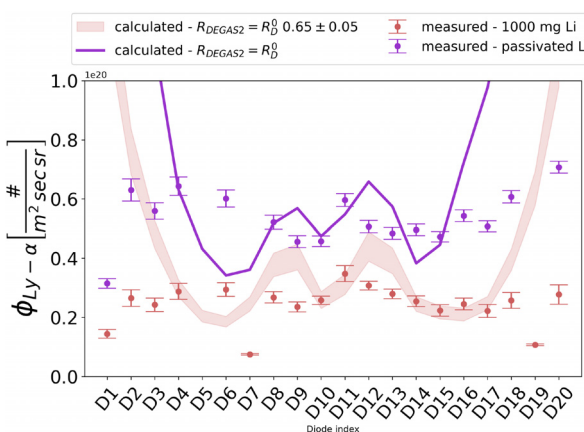


FIG. 10. A comparison of DEGAS2 estimated line integrated Lyman- α intensity with intensity measured using the LTX- β poloidal Lyman- α array at 468 ms, for the 1000 mg Li discharge from the similar density dataset ($R \sim 0.65 \pm 0.05 R_D^0$), shown in red and the passivated lithium case, shown in purple. R_D^0 is the DEGAS2 estimated recycling coefficient for the passivated lithium base case at 468 ms.

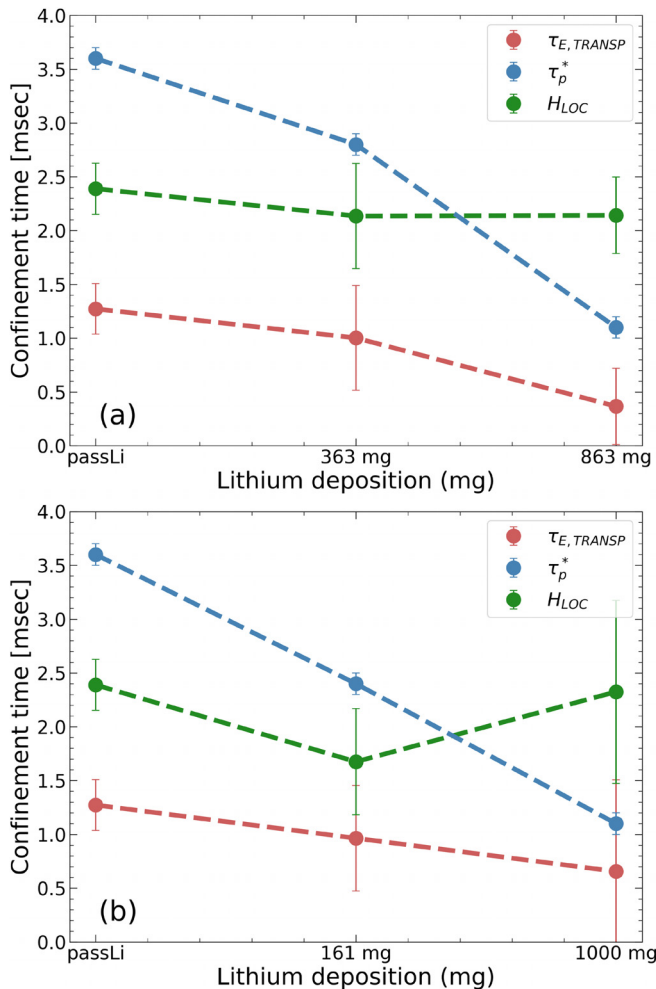


FIG. 11. Comparison of τ_p^* and $\tau_{E,TRANSPI}$ for similar fueling data set (a) and similar density data set (b). H_{LOC} is simply the ratio of the energy confinement time, $\tau_{E,TRANSPI}$, and the expected linear Ohmic confinement (LOC) time, $\tau_{E,LOC}$.⁴¹ In all cases, there is significant enhancement over LOC scaling; $\tau_{E,TRANSPI}$ and $\tau_{E,LOC}$ are averaged over the last quarter of the density decay period, corresponding to roughly 1 ms. Even though confinement time is seen to slightly decrease with increased lithium and reduced density, H_{LOC} stays high, indicating a loss in density due to lithium does not result in a commensurate loss in relative confinement.

defined as the ratio of collision frequency to the high field side to high-field-side bounce frequency,⁴⁵ can be estimated to be between near unity to two orders of magnitude below unity. TRANSP predicted ion collisionality also follows a similar trend, between unity and ~ 0.1 . This indicates that for the low recycling case at least, fluid approximations must break down in the SOL. Since collisional mean free path scales as T^2 , at higher power, and consequently at higher edge temperatures, this effect will be more pronounced. Lower ion collisionality at the edge will lead to mirror trapping along open field lines, which would then force the plasma to develop a potential along the open field lines to maintain ambipolarity and retain electrons.²⁸ Such a potential is called the Pastukhov potential in mirrors. For a tokamak, since the potential depends on the mirror ratio, which is a function of the

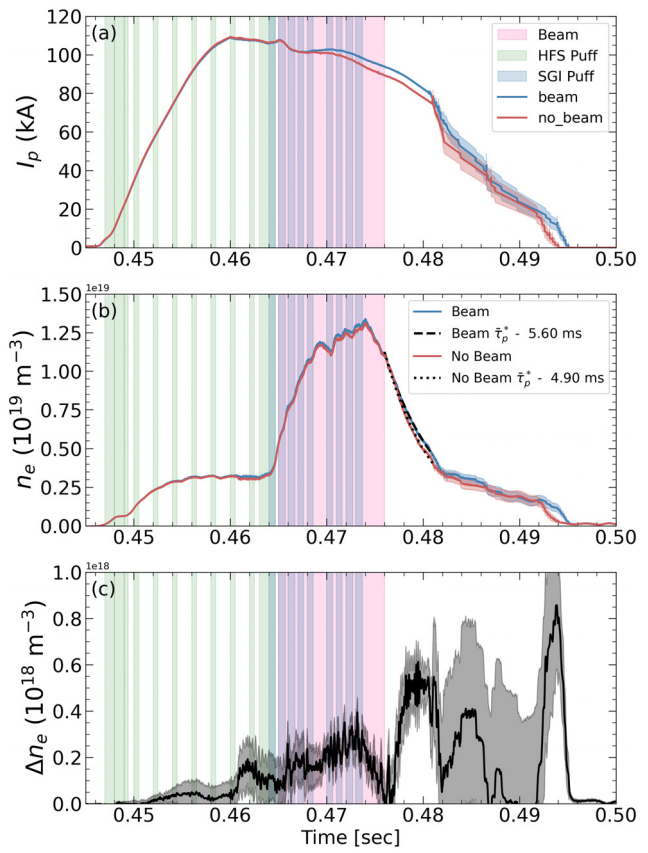


FIG. 12. Discharge characteristics of a beam fueling discharge after lithium deposition. (a) Shows the plasma current, (b) shows line-averaged density, and (c) shows the difference in density between beam and no beam.

polaroidal angle, the effect would manifest as a poloidal electric field. The ions that do escape from the end of the mirror's loss cone, at the high field side, would be hotter, and consequently implant deeper, leading to even better retention in lithium.

Gyrokinetic simulations of open field lines for the passivated lithium base case and the 863 mg low recycling case have been initiated using Gkeyll.⁴⁶ The geometry of the simulation is depicted in Fig. 13. Specifically, Gkeyll is used to solve the long wavelength electromagnetic gyrokinetic equation in the electrostatic limit in one position-space dimension along a single field line in the SOL and two velocity dimensions (1x2v).⁴⁷⁻⁴⁹ A conducting sheath boundary condition is imposed at the end points and the simulations are allowed to run to a steady state. Gkeyll calculated ion distributions at the low-field-side midplane are depicted in Fig. 14, and a mirror boundary using the following equation is overlaid on both distributions and indicates trapping for the 863 mg case

$$\mu > \frac{m_i v_{\parallel}^2}{2B} \left(\frac{1}{R_m} - 1 \right), \quad (4)$$

where R_m is simply the ratio of high-field to low-field-side magnetic field strength, and other symbols have their usual definitions.

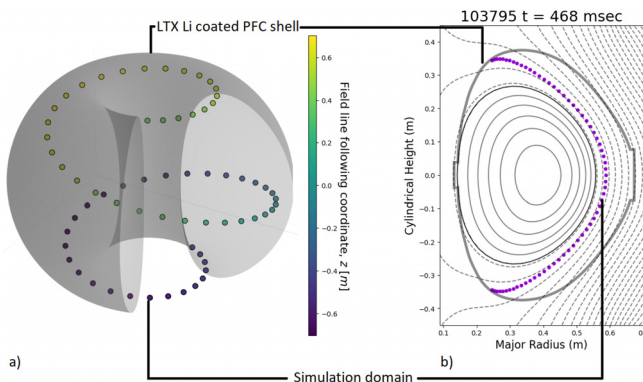


FIG. 13. Simulation geometry of the 1x2v open-field-line Gkeyll simulations, (a) shows the full 3D view of the open field line with respect the LTX- β shells, (b) shows the open field line collapsed on a 2D poloidal plane, overlaid with the kinetic equilibrium of the passivated lithium base case at 468 ms. For these shots, banana width at the low-field-side midplane is estimated using the expression $w_b = \sqrt{\epsilon} \rho_{pol}$,⁴⁴ to be between 1 and 2 cm, whereas the gap between the LCFS and the wall 6–12 cm.

Flow reduction along field lines is well understood for magnetic mirrors, where axial confinement time τ_a is defined as the time an ion will reside along a field line before exiting the mirror. The axial confinement time for a collisionless mirror is a linear function of the ion-ion collision time $\tau_a = \tau_{ii} \log(R_m)$.⁵⁰ For LTX- β , τ_a is analogous to the particle residence time along an open field line, $\tau_{||}$, ignoring the effect of field curvature. Figure 15 depicts the particle residence time along

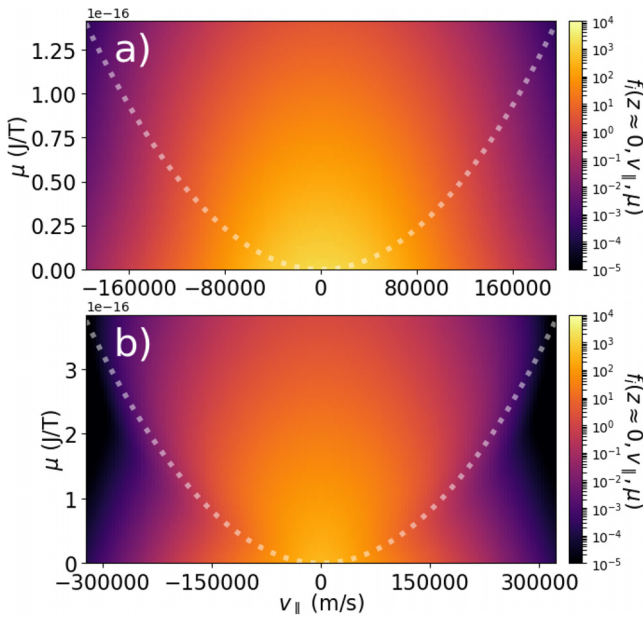


FIG. 14. Ion distributions as a function of μ and $v_{||}$ calculated at the midplane, (a) passivated lithium base case, (b) 863 mg lithium low recycling case. A mirror boundary computed using magnetic field from the kinetic equilibrium is overlaid on both plots. A significant portion of the distribution for the 863 mg case is seen to lie within the boundary.

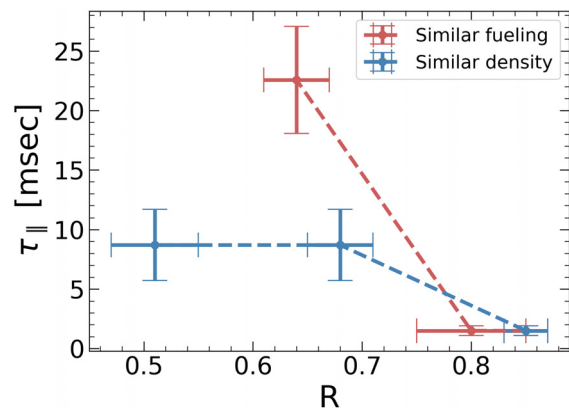


FIG. 15. Ion residence time along an open field line, close to the LCFS [$\tau_{||} = \tau_{ii} \log(R_m)$] as a function of recycling coefficient for the two data sets.

an open field line as a function of recycling coefficient for LTX- β . Ion-ion collision times are estimated using plasma density at the LCFS, as measured using the Thomson scattering system, Fig. 7, and an ion temperature between 0.33 and $0.5 \times T_{e,LCF}$.

Calculating the axial residence times for the low recycling cases leads to values much larger than the residence time of ions in a collisional SOL. In a collisional SOL, for a similar ion temperature range, the ion residence time will simply be the ratio of the connection length to the ion thermal speed or L_c/v_{th} ; this is estimated to be between 0.08 and 0.15 ms. So far, the discussion ignores other effects that may be important, such as field line curvature-induced guiding center drift, and ion-neutral collision time scales. The timescale of curvature-induced guiding center drift should be $\tau_{R_c} = L_v/v_R$, where v_R is the curvature-induced drift velocity, $v_R \propto \frac{m_i v_f^2}{R_c B}$.⁵¹ For this temperature range, using the minor radius of the device as a radius of curvature, τ_{R_c} can be estimated to be between 1.6 and 3.9 ms. The dominant contributor to ion-neutral collisions is the charge exchange between hydrogen atoms and ions.⁵² The characteristic charge exchange time is defined by the following expression, reproduced from,⁵³

$$\tau_{cx} = \frac{1}{\langle \sigma_{cx}(v_f) v_f \rangle n_0}. \quad (5)$$

The cross section σ_{cx} is well documented for a range of energies,⁵⁴ n_0 is the neutral density, and v_f in this case is just the thermal velocity of the hydrogen ions since neutrals are likely cold. For the low recycling set of discharges, the neutral density in SOL is $\sim 1\text{--}5 \times 10^{16} \text{ m}^{-3}$. Assuming ion temperatures are in the range $0.33\text{--}0.5 T_{e,LCF}$, we end up with charge exchange lifetimes of 0.8–4 ms, again, values much larger than a collisional SOL residence time.

Assuming the power crossing into the SOL is constant as we go from high to low recycling, the SOL plasma should increase in temperature and reduce in density. The Larmor radii in this case should be larger, effectively smearing the heat flux footprint over a larger area, the increase in the heat flux width, or λ_q would scale as $\sqrt{T_{edge}}$. Additionally, a low recycling SOL with low enough collisionality will end up with mirror-trapped ions along open field lines, and this trapped population will force the plasma to develop a potential along the open field line, to retain electrons and to maintain ambipolarity,

giving rise to the poloidal electric field along open field lines. The poloidal electric field together with the toroidal B field at the edge will enhance radial transport. Reduced transport along open field lines due to mirror trapping and enhanced radial transport across open field lines should further enhance the broadening of the heat flux footprint. Although questions remain regarding how this scenario will scale for reactor-relevant conditions, specifically regarding how some of the competing effects such as charge exchange and guiding center drifts in the SOL will effect heat transport in a low recycling tokamak. The regime presents a possible solution to one of the most difficult problems facing practical fusion reactors.^{55–58}

V. SUMMARY AND CONCLUSION

This paper documents the performance improvement as a function of lithium evaporation in LTX- β . In general, plasma performance is seen to increase with more lithium deposited on the walls, as seen by various plasma diagnostics. Plasma current is seen to increase, density is seen to drop in the constant fueling scenario, and more fuel is needed to sustain a similar density, as seen in the similar density dataset. Impurity emission is seen to reduce as is neutral hydrogen population as indicated by a general decrease in Lyman- α emission. The improvement in performance presents itself with hotter plasma temperatures at the LCFS. However, the energy confinement time significantly exceeds linear Ohmic confinement (LOC) scaling even for passivated lithium walls, and does not show a consistent improvement with further lithium deposition. The absolute recycling coefficients are found to be in the range of 0.47–0.87. For the lower recycling cases, R is in the range of 0.5–0.6 and the ratio $T_e^{\text{edge}}/T_e^{\text{core}}$ is found to be in the range of 0.4–0.6. It is also demonstrated that as recycling is reduced the effective particle confinement time converges to the TRANSP-predicted energy confinement time. Edge density and temperature for the low recycling cases are found to be in a range that negates the possibility of using fluid models to estimate SOL transport. 1D gyrokinetic simulations predict significant mirror trapping along open field lines for the low recycling case compared to the high recycling case. Such mirror trapping along with a hot edge is expected to reduce transport along open field lines and enhance radial transport in the SOL, which should mitigate heat flux to the PFCs.

ACKNOWLEDGMENTS

The authors acknowledge support from the entire past and present LTX- β team, especially J. Armeli, D. Corl, T. Kozub, E. Merino, F. Rabanales, P. Sloboda, and G. Zimmer. This material is based on the work supported by the U.S. Department of Energy, Office of Science, Office of Fusion Energy Sciences, under Award Nos. DE-AC02-09CH11466, DE-AC05-00OR22725, DE-AC52-07NA27344, DE-SC0023481, DE-SC0019006, DE-SC0019239, and DE-SC0019308. This report was prepared as an account of work sponsored by an agency of the United States Government. Neither the United States Government nor any agency thereof, nor any of their employees, makes any warranty, express, or implied, or assumes any legal liability or responsibility for the accuracy, completeness, or usefulness of any information, apparatus, product, or process disclosed, or represents that its use would not infringe privately owned rights. Reference herein to any specific commercial product, process, or service by trade name, trademark, manufacturer, or otherwise does not necessarily constitute or imply

its endorsement, recommendation, or favoring by the United States Government or any agency thereof. The views and opinions of authors expressed herein do not necessarily state or reflect those of the United States Government or any agency thereof.

AUTHOR DECLARATIONS

Conflict of Interest

The authors have no conflicts to disclose.

Author Contributions

A. Maan: Conceptualization (equal); Data curation (equal); Formal analysis (equal); Investigation (equal); Methodology (equal); Validation (equal); Visualization (equal); Writing – original draft (equal); Writing – review & editing (equal). **D. P. Boyle:** Conceptualization (equal); Data curation (equal); Formal analysis (equal); Investigation (equal); Methodology (equal); Software (equal); Validation (equal); Writing – original draft (equal); Writing – review & editing (equal). **R. Majeski:** Conceptualization (equal); Funding acquisition (equal); Investigation (equal); Project administration (equal); Resources (equal); Supervision (equal); Writing – original draft (equal); Writing – review & editing (equal). **G. J. Wilkie:** Data curation (equal); Formal analysis (equal); Investigation (equal); Methodology (equal); Software (equal); Supervision (equal); Validation (equal); Visualization (equal); Writing – original draft (equal). **M. Francisquez:** Data curation (equal); Formal analysis (equal); Investigation (equal); Software (equal); Supervision (equal); Validation (equal); Visualization (equal); Writing – original draft (equal); Writing – review & editing (equal). **S. Banerjee:** Data curation (equal); Formal analysis (equal); Investigation (equal); Methodology (equal); Validation (equal); Visualization (equal); Writing – original draft (equal); Writing – review & editing (equal). **R. Kaita:** Conceptualization (equal); Project administration (equal); Resources (equal); Supervision (equal); Writing – original draft (equal); Writing – review & editing (equal). **R. Maingi:** Funding acquisition (equal); Project administration (equal); Resources (equal); Supervision (equal); Writing – original draft (equal); Writing – review & editing (equal). **B. P. LeBlanc:** Data curation (equal); Formal analysis (equal). **S. Abe:** Data curation (equal); Formal analysis (equal). **E. Jung:** Data curation (equal); Formal analysis (equal). **E. Perez:** Data curation (equal); Formal analysis (equal); Investigation (equal); Software (equal); Visualization (equal). **W. Capecci:** Data curation (equal); Formal analysis (equal); Investigation (equal); Resources (equal); Supervision (equal); Visualization (equal). **E. T. Ostrowski:** Data curation (equal); Formal analysis (equal); Investigation (equal); Methodology (equal); Visualization (equal); Writing – original draft (equal); Writing – review & editing (equal). **D. B. Elliott:** Data curation (equal); Formal analysis (equal); Resources (equal); Supervision (equal); Validation (equal). **C. Hansen:** Data curation (equal); Formal analysis (equal); Resources (equal); Software (equal); Supervision (equal); Visualization (equal). **S. Kubota:** Data curation (equal); Formal analysis (equal); Investigation (equal); Methodology (equal); Validation (equal); Visualization (equal). **V. Soukhanovskii:** Data curation (equal); Formal analysis (equal); Investigation (equal); Methodology (equal); Supervision (equal); Validation (equal). **L. Zakharov:** Conceptualization (equal); Investigation (equal); Resources (equal); Software (equal); Supervision (equal); Validation (equal).

DATA AVAILABILITY

The data that support the findings of this study are openly available in GitHub at <https://github.com/as-maan/pop23>, Ref. 59.

REFERENCES

- ¹G. McCracken and P. Stott, *Nucl. Fusion* **19**, 889 (1979).
- ²M. Rieth, S. Dudarev, S. Gonzalez de Vicente, J. Alktaa, T. Ahlgren, S. Antusch, D. Armstrong, M. Balden, N. Baluc, M.-F. Barthe, W. Basuki, M. Battabyal, C. Becquart, D. Blagoeva, H. Boldyryeva, J. Brinkmann, M. Celino, L. Ciupinski, J. Correia, A. De Backer, C. Domain, E. Gaganidze, C. García-Rosales, J. Gibson, M. Gilbert, S. Giusepponi, B. Gludovatz, H. Greuner, K. Heinola, T. Höschens, A. Hoffmann, N. Holstein, F. Koch, W. Krauss, H. Li, S. Lindig, J. Linke, C. Linsmeier, P. López-Ruiz, H. Maier, J. Matejicek, T. Mishra, M. Muhammed, A. Muñoz, M. Muzyk, K. Nordlund, D. Nguyen-Manh, J. Opschoor, N. Ordás, T. Palacios, G. Pintsuk, R. Pippian, J. Reiser, J. Riesch, S. Roberts, L. Romaner, M. Rosiński, M. Sanchez, W. Schulmeyer, H. Traxler, A. Ureña, J. van der Laan, L. Veleva, S. Wahlberg, M. Walter, T. Weber, T. Weitkamp, S. Wurster, M. Yar, J. You, and A. Zivelonghi, *J. Nucl. Mater.* **432**, 482 (2013).
- ³A. de Castro, C. Moynihan, S. Stemmley, M. Szott, and D. N. Ruzic, *Phys. Plasmas* **28**, 050901 (2021).
- ⁴M. Christenson, “The design and development of hydrogen isotope extraction technologies for a limit-style liquid lithium loop,” Ph.D. thesis (University of Illinois, Urbana-Champaign, 2018).
- ⁵M. Ono, R. Majeski, M. Jaworski, Y. Hirooka, R. Kaita, T. Gray, R. Maingi, C. Skinner, M. Christenson, and D. Ruzic, *Nucl. Fusion* **57**, 116056 (2017).
- ⁶M. Baldwin, R. Doerner, S. Luckhardt, and R. Conn, *Nucl. Fusion* **42**, 1318 (2002).
- ⁷W. Capecchi, J. Anderson, D. Boyle, P. Hughes, A. Maan, R. Majeski, D. Elliott, and C. Hansen, *Nucl. Fusion* **61**, 126014 (2021).
- ⁸P. E. Hughes, W. Capecchi, D. B. Elliott, L. E. Zakharov, R. E. Bell, C. Hansen, D. P. Boyle, S. N. Gorelenkov, R. Majeski, and R. Kaita, *Plasma Phys. Controlled Fusion* **63**, 085020 (2021).
- ⁹S. Kubota, R. Majeski, D. P. Boyle, R. Kaita, T. Kozub, R. Lantsov, E. Merino, X. V. Nguyen, W. A. Peebles, and T. L. Rhodes, *Rev. Sci. Instrum.* **89**, 10H114 (2018).
- ¹⁰T. Gray, R. Kaita, R. Majeski, J. Spaleta, and J. Timberlake, *Rev. Sci. Instrum.* **77**, 10E901 (2006).
- ¹¹A. Maan, D. Boyle, R. Majeski, S. Banerjee, M. Francisquez, R. Kaita, G. Wilkie, W. Capecchi, S. Kubota, C. Hansen, and V. Soukhanovskii, *Nucl. Mater. Energy* **35**, 101408 (2023).
- ¹²L. Zakharov, N. Gorelenkov, R. White, S. Krasheninnikov, and G. Pereverzev, *Fusion Eng. Des.* **72**, 149 (2004).
- ¹³S. I. Krasheninnikov, L. E. Zakharov, and G. V. Pereverzev, *Phys. Plasmas* **10**, 1678 (2003).
- ¹⁴P. J. Catto and R. D. Hazeltine, *Phys. Plasmas* **13**, 122508 (2006).
- ¹⁵R. Maingi, D. Boyle, J. Canik, S. Kaye, C. Skinner, J. Allain, M. Bell, R. Bell, S. Gerhardt, T. Gray, M. Jaworski, R. Kaita, H. Kugel, B. LeBlanc, J. Manickam, D. Mansfield, J. Menard, T. Osborne, R. Raman, A. Roquemore, S. Sabbagh, P. Snyder, and V. Soukhanovskii, *Nucl. Fusion* **52**, 083001 (2012).
- ¹⁶A. J. Wootton, B. A. Carreras, H. Matsumoto, K. McGuire, W. A. Peebles, C. P. Ritz, P. W. Terry, and S. J. Zweben, *Phys. Fluids B* **2**, 2879 (1990).
- ¹⁷P. Helander and D. J. Sigmar, *Collisional Transport in Magnetized Plasmas* (Cambridge University Press, Cambridge, UK, 2005).
- ¹⁸J. L. Weiland, *Collective Modes in Inhomogeneous Plasma: Kinetic and Advanced Fluid Theory* (Institute of Physics, Bristol, UK, 2000), see <https://catalog.lib.uchicago.edu/uvcfind/Record/4123064>.
- ¹⁹R. Kaita, *Plasma Phys. Controlled Fusion* **61**, 113001 (2019).
- ²⁰J. Snipes, E. Marmar, J. Terry, M. Bell, R. Budny, K. Hill, D. Jassby, D. Mansfield, D. Meade, H. Park, J. Strachan, B. Stratton, E. Synakowski, G. Taylor, D. Ruzic, and M. Shaheen, *J. Nucl. Mater.* **196–198**, 686 (1992).
- ²¹D. K. Mansfield, K. W. Hill, J. D. Strachan, M. G. Bell, S. D. Scott, R. Budny, E. S. Marmar, J. A. Snipes, J. L. Terry, S. Batha, R. E. Bell, M. Bitter, C. E. Bush, Z. Chang, D. S. Darrow, D. Ernst, E. Fredrickson, B. Grek, H. W. Herrmann, A. Janos, D. L. Jassby, F. C. Jobes, D. W. Johnson, L. C. Johnson, F. M. Levinton, D. R. Mikkelsen, D. Mueller, D. K. Owens, H. Park, A. T. Ramsey, A. L. Roquemore, C. H. Skinner, T. Stevenson, B. C. Stratton, E. Synakowski, G. Taylor, A. von Halle, S. von Goeler, K. L. Wong, S. J. Zweben, and T. Group, *Phys. Plasmas* **3**, 1892 (1996).
- ²²D. Mansfield, D. Johnson, B. Grek, H. Kugel, M. Bell, R. Bell, R. Budny, C. Bush, E. Fredrickson, K. Hill, D. Jassby, R. Maqueda, H. Park, A. Ramsey, E. Synakowski, G. Taylor, and G. Wurden, *Nucl. Fusion* **41**, 1823 (2001).
- ²³S. V. Mirnov, E. A. Azizov, V. A. Evtikhin, V. B. Lazarev, I. E. Lyublinski, A. V. Vertkov, and D. Y. Prokhorov, *Plasma Phys. Controlled Fusion* **48**, 821 (2006).
- ²⁴V. Evtikhin, A. Vertkov, I. Lyublinski, B. Khripunov, V. Petrov, and S. Mirnov, *J. Nucl. Mater.* **307–311**, 1664 (2002).
- ²⁵H. Gerhauser, R. Zagórski, H. Claaßen, G. Mank, T. Loarer, J. Gunn, and C. Boucher, *Nucl. Fusion* **42**, 805 (2002).
- ²⁶M. Apicella, G. Mazzitelli, V. Pericoli Ridolfini, V. Lazarev, A. Alekseyev, A. Vertkov, and R. Zagórski, *J. Nucl. Mater.* **363–365**, 1346 (2007).
- ²⁷D. P. Boyle, R. Majeski, J. C. Schmitt, C. Hansen, R. Kaita, S. Kubota, M. Lucia, and T. D. Rognlien, *Phys. Rev. Lett.* **119**, 015001 (2017).
- ²⁸R. Majeski, R. E. Bell, D. P. Boyle, R. Kaita, T. Kozub, B. P. LeBlanc, M. Lucia, R. Maingi, E. Merino, Y. Raitses, J. C. Schmitt, J. P. Allain, F. Bedoya, J. Bialek, T. M. Biewer, J. M. Canik, L. Buzzi, B. E. Koel, M. I. Patino, A. M. Capecchi, C. Hansen, T. Jarboe, S. Kubota, W. A. Peebles, and K. Tritz, *Phys. Plasmas* **24**, 056110 (2017).
- ²⁹A. Maan, R. Kaita, E. T. Ostrowski, R. Majeski, D. P. Boyle, D. C. Donovan, R. A. Ellis, B. E. Koel, and T. M. Biewer, *Rev. Sci. Instrum.* **91**, 026104 (2020).
- ³⁰A. Maan, E. Ostrowski, R. Kaita, D. Donovan, R. Majeski, D. Boyle, P. Hughes, E. Merino, T. Kozub, B. E. Koel, D. Elliott, T. Biewer, F. Scotti, V. Soukhanovskii, and R. Lunsford, *IEEE Trans. Plasma Sci.* **48**, 1463 (2020).
- ³¹D. Boyle, J. Anderson, S. Banerjee, R. Bell, W. Capecchi, D. Elliott, C. Hansen, S. Kubota, B. LeBlanc, A. Maan, R. Maingi, R. Majeski, J. Menard, S. Oliva, T. Rhodes, V. Soukhanovskii, and L. Zakharov, *Nucl. Fusion* **63**, 056020 (2023).
- ³²J. Hoenigman and R. Keil, *Appl. Surf. Sci.* **18**, 207 (1984).
- ³³R. Sullenberger, “Uptake and retention of residual vacuum gases in lithium and lithium films,” Master’s thesis (Princeton University, 2012).
- ³⁴A. Maan, D. P. Boyle, R. Kaita, E. T. Ostrowski, D. C. Donovan, R. P. Majeski, B. E. Koel, T. M. Biewer, P. E. Hughes, C. Hansen, S. Kubota, and V. Soukhanovskii, *Plasma Phys. Controlled Fusion* **63**, 025007 (2020).
- ³⁵R. Kaita, M. Lucia, J. Allain, F. Bedoya, R. Bell, D. Boyle, A. Capecchi, M. Jaworski, B. Koel, R. Majeski, J. Roszell, J. Schmitt, F. Scotti, C. Skinner, and V. Soukhanovskii, *Fusion Eng. Des.* **117**, 135 (2017).
- ³⁶S. Tsuji, *Fusion Eng. Des.* **15**, 311 (1991).
- ³⁷D. Stotler, C. Karney, R. Kanzleiter, and S. Jaishankar, see <https://w3.pppl.gov/degas2/> for “Degas 2 user’s manual” (2020).
- ³⁸C. Hansen, D. P. Boyle, J. C. Schmitt, and R. Majeski, *Phys. Plasmas* **24**, 042513 (2017).
- ³⁹P. C. Stangeby, *The Plasma Boundary of Magnetic Fusion Devices. Series: Series in Plasma Physics*, edited by Peter Stangeby (Taylor & Francis, 2002), Vol. 7.
- ⁴⁰F. M. Laggner, A. Bortolon, A. M. Rosenthal, T. M. Wilks, J. W. Hughes, C. Freeman, T. Golfinopoulos, A. Nagy, D. Mauzey, M. W. Shafer, and DIII-D Team, *Rev. Sci. Instrum.* **92**, 033522 (2021).
- ⁴¹R. J. Goldston, *Plasma Phys. Controlled Fusion* **26**, 87 (1984).
- ⁴²R. Penrose, *Math. Proc. Cambridge Philos. Soc.* **52**, 17–19 (1956).
- ⁴³J. Breslau, M. Gorelenkova, F. Poli, J. Sachdev, A. Pankin, G. Perumpilly, X. Yuan, and L. Glant, see <https://doi.org/10.11578/dc.20180627.4> for “TRANSP” (2018).
- ⁴⁴R. Hawryluk, *Physics of Plasmas Close to Thermonuclear Conditions*, edited by B. Coppi, G. Leotta, D. Pfirsich, R. Pozzoli, and E. Sindoni (Pergamon, 1981), pp. 19–46.
- ⁴⁵P. Helander and D. J. Sigmar, *Connaissance Des Temps* (Cambridge University Press, 2005).
- ⁴⁶T. G. Team, see <http://gkeyll.readthedocs.io/> for “The Gkeyll code” (2022).
- ⁴⁷N. R. Mandell, “Magnetic fluctuations in gyrokinetic simulations of tokamak scrape-off layer turbulence,” Ph.D. thesis (Princeton University, 2021).
- ⁴⁸M. Francisquez, N. R. Mandell, A. Hakim, and G. W. Hammett, “Mapped discontinuous Galerkin interpolations and sheared boundary conditions,” [arXiv:2110.02249](https://arxiv.org/abs/2110.02249) (2021).
- ⁴⁹T. N. Bernard, F. D. Halpern, M. Francisquez, N. R. Mandell, J. Juno, G. W. Hammett, A. Hakim, G. Wilkie, and J. Gutierl, “Kinetic modeling of neutral transport for a continuum gyrokinetic code,” [arXiv:2202.00811](https://arxiv.org/abs/2202.00811) (2022).

- ⁵⁰A. Wong, G. Dimonte, J. Ferron, M. Fukao, K. Jones, A. Kuthi, K. Lam, B. Leikind, R. Schumacher, H. Stephanian, and R. Suchannek, *Nucl. Instrum. Methods Phys. Res.* **207**, 207–221 (1983).
- ⁵¹J. D. Huba, “NRL (Naval Research Laboratory) plasma formulary, revised” (2007), see <https://www.nrlnavy.mil/News-Media/Publications/NRL-Plasma-Formulary/>
- ⁵²J. Cornelis, R. Sporken, G. van Oost, and R. Weynants, *Nucl. Fusion* **34**, 171 (1994).
- ⁵³F. Jaulmes, G. Zadvitskiy, K. Bogar, M. Imrisek, J. Hromadka, S. Cats, J. Varju, M. Komm, and R. Panek, *Nucl. Fusion* **61**, 046012 (2021).
- ⁵⁴R. K. Janev, U. Samm, and D. Reiter, “Collision processes in low-temperature hydrogen plasmas,” IAEA Report No. JUEL-4105 (2003), see <https://inis.iaea.org/search/searchsinglerecord.aspx?recordsFor=SingleRecord&RN=35040310>.
- ⁵⁵R. Goldston, *Nucl. Fusion* **52**, 013009 (2011).
- ⁵⁶B. Chen, X. Xu, T. Xia, M. Porkolab, E. Edlund, B. LaBombard, J. Terry, J. Hughes, S. Mao, M. Ye, and Y. Wan, *Nucl. Fusion* **57**, 116025 (2017).
- ⁵⁷C. Chang, S. Ku, A. Loarte, V. Parail, F. Köchl, M. Romanelli, R. Maingi, J.-W. Ahn, T. Gray, J. Hughes, B. LaBombard, T. Leonard, M. Makowski, and J. Terry, *Nucl. Fusion* **57**, 116023 (2017).
- ⁵⁸T. Eich, A. Leonard, R. Pitts, W. Fundamenski, R. Goldston, T. Gray, A. Herrmann, A. Kirk, A. Kallenbach, O. Kardaun, A. Kukushkin, B. LaBombard, R. Maingi, M. Makowski, A. Scarabosio, B. Sieglin, J. Terry, A. Thornton, A. U. Team, and J. E. Contributors, *Nucl. Fusion* **53**, 093031 (2013).
- ⁵⁹A. Maan, “Raw data and figures for estimates of global recycling coefficients for LTX- β discharges,” GitHub (2023), <https://github.com/as-maan/pop23>